Title: Exceptional longevity of mammalian ovarian and oocyte macromolecules throughout the reproductive lifespan

Authors:

Ewa K. Bomba-Warczak[1]†, Karen M. Velez[2]†, Luhan T Zhou[2], Christelle Guillermier[4], Seby Edassery[1], Matthew L. Steinhauser[4], Jeffrey N. Savas[1]*, Francesca E. Duncan [2]*

Affiliations:

[1]Department of Neurology, Northwestern University Feinberg School of Medicine, Chicago, IL.
[2]Department of Obstetrics and Gynecology, Feinberg School of Medicine, Northwestern University, Chicago, IL.
[3]Department of Medicine, Aging Institute, University of Pittsburgh School of Medicine, Pittsburgh, PA.
[4]Department of Medicine, Division of Genetics, Brigham and Women's Hospital, Boston, MA.

†These authors contributed equally to this work.

*Corresponding authors: Emails: f-duncan@northwestern.edu and jeffrey.savas@northwestern.edu

Abstract:

The mechanisms contributing to age-related deterioration of the female reproductive system are complex, however aberrant protein homeostasis is a major contributor. We elucidated exceptionally stable proteins, structures, and macromolecules that persist in mammalian ovaries and gametes across the reproductive lifespan. Ovaries exhibit localized structural and cell-type specific enrichment of stable macromolecules in both the follicular and extrafollicular environments. Moreover, ovaries and oocytes both harbor a panel of exceptionally long-lived proteins, including cytoskeletal, mitochondrial, and oocyte-derived proteins. The exceptional persistence of these long-lived molecules suggest a critical role in lifelong maintenance and age-dependent deterioration of reproductive tissues.

One sentence summary:

Exceptionally long-lived macromolecules in mammalian ovaries and oocytes as pillars for lifelong reproductive health span.

Main Text:

The female reproductive system is the first to age in the human body with fertility decreasing for women in their mid-thirties and reproductive function ceasing completely at menopause (*1*). In the ovary, aging is associated with a loss in gamete quantity and quality which contributes to infertility, miscarriages, and birth defects (*2-5*). Moreover, the age-dependent loss of the ovarian hormone, estrogen, has adverse general health outcomes (*6*). These sequelae are significant as women globally are delaying childbearing and the gap between menopause and lifespan is widening due to medical interventions (*7, 8*). Although aging is a multifaceted process, loss of proteostasis and dysfunctional protein quality control pathways are hallmarks of reproductive aging (*9*).

Proteostasis relies on tight inter-regulation of protein synthesis, post-translational modifications, folding, and degradation (*10*). While most protein lifetimes in mammals fall within the scale from hours to days

(*11, 12*), a subset of intracellular proteins persists for months in rodents (*13, 14*). These long-lived proteins (LLPs) are enriched in tissues harboring long-lived post-mitotic terminally differentiated cells, such as the brain and heart (*13-15*). Although the extended lifespan of LLPs places them at inherent risk for accumulating damage during aging, many of them provide key structural support for the lifelong maintenance of highly stable protein complexes in cells (*16*).

The mammalian ovary is comprised of a fixed and nonrenewable pool of long-lived cells or oocytes. In humans, oocytes initiate meiosis during fetal development, and by birth, all oocytes are arrested at prophase of meiosis I (*17, 18*). This cell cycle arrest is maintained until ovulation, which occurs any time between puberty and menopause, and thus can span decades. The oocytes are particularly sensitive to protein metabolism alterations because they contribute the bulk cytoplasm to the embryo following fertilization. Thus, maternal proteins produced during oogenesis are essential to generate high-quality gametes (*9*). The ovarian microenvironment is a critical determinant of gamete quality and has been shown to become fibro-inflamed and stiff with age (*19-21*). Although a small number of oocyte-specific proteins have been identified as long-lived, including cohesins and several centromere-specific histones, there has not been a discovery-based approach to define the long-lived proteome of the ovary and oocyte. Thus, the potential contribution of LLPs to the age-related deterioration of the reproductive system in mammals remains to be elucidated. In this study we used multi-generational whole animal metabolic stable isotope labeling and leading mass spectrometry (MS)-based quantitative proteomic approaches to visualize and identify ovarian and oocyte long lived macromolecules in *vivo* during milestones relevant to the reproductive system.

Exceptional longevity of ovarian structures and molecules in mammals.

The mammalian ovary is a structurally complex, heterogenous, and dynamic organ with follicles at different stages of development, remnants of ovulation (corpora lutea), and a heterogeneous stroma (*22*) (**Fig. 1A**). Very little is known about the long-term homeostasis and relative turnover of the ovarian tissue components during aging. To address this, we visualized the lifespan of ovarian macromolecules in mammals using a combination of stable isotope labelling and multi-isotope imaging mass spectrometry (MIMS) **(fig. S1A).** First, using a two-generational metabolic labelling of animals with ^{15}N, we generated a cohort of fully ^{15}N-labelled pups. After birth, labelled females were kept with the labelled dam until weaning, at which time their food source was switched to the ^{14}N-chow chase. Using previously established methods (*9, 23-25*), we determined that chase periods of 6 and 10 months represented a biologically relevant reproductive aging continuum as mice within this age range begin to manifest ovarian aging phenotypes, including follicle loss (**fig. S1 B-D)**, decreased ovulation (**fig. S1 E and F)**, and increased fibrotic foci in the ovarian stroma (**fig. S1 G-J**). Importantly, sufficient numbers of oocytes can still be collected at these timepoints for meaningful further downstream analyses of this rare cell type. We first performed MIMS on ovarian sections to visualize and quantify the abundance of ^{14}N, representing molecules which have been replaced during the chase period (blue-teal), and ^{15}N, which represents ^{15}N-containing molecules that must have persisted through the chase period and therefore are long-lived (orange-pink) (**Figs. 1B, S2 A and B**) (*26-28*). Within the ovarian follicles, MIMS revealed a strikingly higher abundance of ^{15}N containing molecules in primordial and primary stages relative to later stage follicles, suggesting that primordial follicles can persist for months with limited macromolecular turnover (**Fig. 1C**). As follicles progress through the primary, secondary, and antral stages the $^{15}N/^{14}N$ ratio decreases due to signal dilution associated with the increase of cell number and follicle growth (**Figs. 1C, S2 C**). This change in ^{15}N abundance was most apparent in the granulosa cells where long-lived molecules were significantly higher in those within primordial and primary follicles compared to later follicle stages (**Fig. 1C** and **F**). In addition to granulosa cells, long-lived molecules also localized to the basement membrane of some early growing follicles (**fig. S1D**). Beyond the follicle, other somatic compartments of the ovary were additionally found to have higher ^{15}N:^{14}N ratio suggesting enrichment in long-lived

components, including steroidogenic cells (theca layer and corpora lutea), stromal cells, and cells within the ovarian surface epithelium (OSE) (**Fig. 1 B** and **D**). Our quantitative analysis revealed that the OSE had significantly higher $^{15}N/^{14}N$ ratio among the mentioned cell types (**Fig. 1G**). Lastly, we analyzed the $^{15}N/^{14}N$ ratios in the nucleus relative to the cytoplasm, which revealed significant enrichment of long-lived, ^{15}N- positive molecules in the nuclei of granulosa cells within primary follicles, and cells within the corpora lutea, the stroma, and the OSE. (**Fig. 1 E** and **H**). As both proteins and nucleic acids contain nitrogen, the ^{15}N-positive nuclear signal could correspond to known long-lived nuclear proteins, such as histones, nuclear pore proteins, and lamins, which were previously identified in neuronal, post-mitotic cells (*14, 15*). Alternatively, as these nuclear ^{15}N-hotspots coincided with the ^{31}P signal, which is enriched in DNA and correlates with DNA labeling(*29*), this data may suggest that the DNA itself is long-lived (**Fig. 1E**). These results reveal that distinct macromolecular components within select ovarian cells and tissue regions persist throughout the healthy reproductive stage, with limited renewal, and those long-lived molecules persist through the stage where ovaries manifest marked reproductive aging phenotypes.

Identification of the long-lived proteome in mammalian ovaries

Although MIMS analysis provides important spatial information on long-lived structures in the ovary, it does not provide the identity of ^{15}N-containing macromolecules that comprise them. To address this, we performed liquid chromatography mass spectrometry (LC-MS/MS)-based proteomic analysis of ovarian tissues isolated from metabolically labeled mice. After 6-months of ^{14}N-chase, we identified 36,222 ± 6768 ^{14}N-peptides mapping to 4106 proteins, and 13 ± 5 ^{15}N peptides, which collectively mapped to 33 LLPs across all the biological replicates (**Fig. 2 A and B, table S1**). To gain a deeper insight into the persistence of LLPs beyond 6 months, we also analyzed ovaries isolated from females that remained on ^{14}N chase for 10 months. Although the total numbers of both ^{14}N and ^{15}N peptides and proteins were similar between the two timepoints (39,637 ± 12005 ^{14}N-peptides mapping to 4464 proteins and 13 ± 6 ^{15}N peptides mapping to 15 LLPs), the majority of LLPs identified at 6 months were no longer identified as long-lived at the 10-month chase timepoint. Only tubulins and select histones persisted and were identified as LLPs at this aged timepoint. Gene ontology (GO) enrichment analysis of LLPs identified at the 6-month chase timepoint revealed significant overrepresentation for terms related to chromatin, nucleosome, tubulin complex, and mitochondria (**Fig. 2C**).

Next, we determined the quantity of each LLP remaining after the ^{14}N-chase period by calculating the fractional abundance (FA; ^{15}N remaining, $^{15}N/[^{14}N + ^{15}N]$) for each LLP in the ovary using reconstructed MS1 chromatograms from LC-MS/MS analysis (*30*) (**Fig. 2 D-F**). We found that LLPs had significant differences in FA between the 6- and 10-month time points, with 1.13 ± 0.08 % and 1.37 ± 0.12 % ^{15}N-remaining, respectively (**Fig. 2D**). The discrete pool of proteins that persisted throughout both time points allowed for a unique direct comparison of ^{15}N to ^{14}N- peptide peak intensities. This analysis showed reduced abundance of ^{15}N at the 10-month chase timepoint, consistent with continual, albeit slow, turnover of the protein pool (**Fig. 2E**). Interestingly, at the 6-month chase timepoint, we identified ^{15}N peptides mapping to an oocyte-specific protein, Zona pellucida-3 protein (ZP3), indicating that a pool persists without turnover for at least 6 months, but less than 10 months, as long-lived ZP3 was no longer identified at the 10-month timepoint (**Fig. 2F**). While histones and tubulin have been previously identified as LLPs in the mammalian brain and heart tissues, the 6-month long persistence of ZP3 in mouse ovaries is unexpected and of potential importance to reproductive biology.

Exceptional longevity of mitochondrial and myosin proteins in mammalian oocytes

MIMS analysis of ovarian sections also captured oocytes at various stages of development, which in addition to the enrichment of ^{15}N-signal within the oocyte nucleus, revealed multiple smaller cytoplasmic ^{15}N-hot spots (**Fig. 3A**). Thus, to determine the identity of these ^{15}N-enriched molecules we isolated fully grown oocytes from ovaries of labeled mice at 6 and 10 months chase timepoints followed by LC-MS/MS

analysis (**Fig. 3B and S3A**). In oocytes, we identified a total of 2919 proteins at 6-months and 3234 proteins at 10-months (**Fig. 3B, table S2**). Although after 6-months of chase, we identified 146 LLPs in oocytes, only 11 LLPs were identified after 10-months, indicating that by this timepoint a vast majority of LLPs have been degraded and renewed. Interestingly, the GO analysis of LLPs in oocytes identified at 6-month timepoint revealed a significant enrichment of terms related to nucleosomes, myosin complex and several additional terms related to mitochondria including - OxPhos complexes, mitochondrial nucleoid, TCA cycle complexes, and mitochondrial permeability transition pore complex (**Fig. 3B**).

Next, we quantified the fraction of each protein pool that persisted for 6 or 10 months by calculating fractional abundance (FA) values, where the higher the value the longer-lived the corresponding proteins are (**fig. S3B**). Overall, there was no significant difference in FA between the two chase timepoints, with 41 ± 2.9 and 50.8 ± 12.2 ^{15}N-remaining at 6 and 10-months, respectively (**fig. S3C**). The higher average FA average at 10-month chase is likely due to turnover of proteins with lower FA values at 6 months, which by 10-months would leave the oocyte with the most persistent pool of proteins. In agreement, the FA values for 4 LLPs that were identified at both time points (Hba, Atp5a, Atp5B, and Hist1h4a) sharply decline between 6 and 10 months (**fig. S3D**), demonstrating protein degradation and replenishment. Considering the high abundance of mitochondrial proteins in our data set, and recent reports showing that expression of mitochondrial proteins is suppressed in aging oocytes (*31*), we compared the number of mitochondrial proteins and spectral counts identified (**fig. S3E and F**), as well as fractional abundance (**fig. S3G**) for mitochondrial proteins across the two timepoints. Our results indicate that while there are no significant differences in total mitochondrial protein abundance at 6- and 10-months post-chase, the pool of long lived mitochondrial proteins decreased significantly, with the majority of proteins being turned over at the later timepoint.

Hierarchical clustering of the LLPs identified at the 6-month timepoint revealed mitochondrial proteins and myosins as the two protein groups with the highest fractional abundance in the oocyte (**Fig. 3C**). In particular, mitochondria exhibited a wide range of FA values ranging from 1.10% to 98.9%, with an average of 55.9 ± 35.1 of ^{15}N-remaing at 6-months (**table S2**). FA values for myosins was markedly higher than both actin and tubulin with an average FA value of 80.97 ± 19.8 % for myosins, 31.4 ± 15.6% for actins, and only 8.3 ± 1.4% for tubulins. This indicates that while all three cytoskeletal components are long-lived, nearly 81% of the myosin protein pool persists throughout the 6-month timepoint, whereas only 31% of actin protein pool and 8.3% of tubulin protein pool persists throughout the same length of time. Histones were also identified as LLPs in oocytes with average FA values of 7.7 ± 9.8. Mitochondrial proteins, histones, myosins, and tubulins have been previously identified as LLPs in brain and heart tissues, which are known to contain long-lived terminally differentiated cells (i.e. neurons in the brain and cardiac myocytes in the heart) (*13*). Importantly, however, this is the first time that a subset of the same proteins has been identified as long lived in the germ cell (**Fig. 3D**). Interestingly, the fractional abundance of mitochondrial LLPs in the brain (10.2 ± 6.6%)(*13*) and myosins in the heart (4.6 ± 8.1%)(*13*) is much lower in than the same LLPs quantified in the oocyte (55.9 ± 35.1)(**Fig. 3D**). In contrast, histones were less long-lived in the oocyte compared to the brain, and there was no significant difference observed for tubulins (**Fig. 3D**). Thus, although the identity of long-lived proteins may be conserved across tissues with long-lived cells, differences in fractional abundance may reflect tissue specific functions and requirements.

Discussion

In this study, multi-generational whole animal metabolic stable isotope labeling, paired with multi modal MS-based quantitative approaches enabled visualization and identification of ovarian and oocyte long lived macromolecules in vivo. Our findings provide a novel framework for how long-lived structures may regulate gamete quality. Long-lived macromolecules localized throughout the ovary including the

197 follicular compartment with prominent signals in the granulosa cells of primordial and primary follicles
198 relative to later stage growing follicles. These findings are consistent with the knowledge that the
199 squamous pre-granulosa cells surrounding the oocyte within primordial follicles form early in
200 development which coincided with the ^{15}N-labelling pulse period. These squamous granulosa cells are
201 generally thought to lack the ability to undergo mitotic division until follicles are activated to grow, so it
202 is not surprising that we observed long lived macromolecules persisting within them (*32*). In contrast,
203 granulosa cells in growing follicles are generated by cell divisions that take place during follicle activation
204 and growth which coincided with the ^{14}N-chase period. Thus, long-lived structures (i.e. enriched with ^{15}N)
205 were diluted through cell divisions during follicle growth. Moreover, during follicle growth, granulosa
206 cells proliferate and differentiate adding new pools of synthesized proteins and molecules. Our results
207 demonstrate that macromolecules formed early in development can persist in squamous granulosa cells
208 for months. Thus, it is possible that these long-lived molecules will accumulate more damage in primordial
209 follicles that remain quiescent for longer periods relative to those that activate earlier. Whether such
210 damage occurs and how it translates into decreased follicle survival or gamete quality will require further
211 investigation.
212
213 Within the extrafollicular ovarian environment, the OSE exhibited a striking enrichment of long-lived
214 molecules. The OSE is highly dynamic due to repeated post-ovulation wound healing and repair, and its
215 regenerative capacity occurs through a somatic stem/progenitor cell-mediated process (*33*). Interestingly,
216 long-lived proteins are retained in other cells undergoing repeated asymmetric divisions and are speculated
217 to contribute to the reproductive aging process (*34*). Consistent with this possibility, the architecture and
218 wound healing ability of the OSE is altered with advanced reproductive age (*35*). Furthermore, nuclear
219 enrichment of the ^{15}N signal was highest in cells of the OSE. It is plausible that the older template DNA
220 is segregated into the daughter cell destined to become the stem cell to ensure genetic stability of the OSE.
221 Better understanding of the dynamics of long lived molecules in the OSE will require generation of
222 specific samples at precise stages of the estrous cycle and across a time course of ovulation to capture
223 follicular rupture and repair.
224
225 Through LC-MS/MS analysis, we identified specific long-lived proteins in the mammalian ovary across
226 the reproductive lifespan. LLPs tend to be part of large protein complexes and include histones, nuclear
227 pore complex proteins, lamins, myelin proteins, and mitochondrial proteins (*16*). In the ovary, the major
228 categories of LLPs included histones, cytoskeletal proteins, and mitochondrial proteins. ZP3 was an
229 oocyte-derived protein identified to be long-lived for at least 6 months. ZP3 is a protein that comprises
230 the zona pellucida (ZP) or glycoprotein matrix of the oocyte, and it is expressed in oocytes of actively
231 growing follicles beginning at the primary stage when the ZP begins to form (*36*). However, during the
232 pulse period, there would have been very few growing follicles in the ovary because of the immature age
233 of the mice, and most importantly, none of these follicles would have persisted 6 months since
234 folliculogenesis only takes approximately 21 days (*37*). These findings suggest that ZP3 may be expressed
235 earlier in oocyte development than previously anticipated. Because LLPs can be at the core of scaffold
236 complexes, a primitive zona may exist at the primordial follicle stage upon which the bona fide ZP is
237 established in growing follicles (*38, 39*). Consistent with this, expression of ZP proteins has been observed
238 in human primordial follicles (*39*). Interestingly, there are documented age-related defects in the structure
239 and function of the ZP which occur with time-dependent scaffold deterioration. An alternate explanation
240 for our observation is that ZPs from atretic follicles persist and become incorporated into the ovarian
241 matrix. Precedent for this exists because ZP proteins have been identified as components of the matrisome
242 of decellularized porcine ovaries (*40*). Interestingly we did not identify ZP3 as an LLP in isolated fully
243 grown oocytes which provides further support that in the ovary, the long-lived pool of ZP3 is derived from
244 primordial follicles or are within the matrix. These possibilities require further investigation and may not
245 be mutually exclusive.

Most LLPs were degraded and replaced between 6-10 months of chase. At the 6 month time point, we detected more long lived proteins than the 10 month time point in both the ovary and the oocyte because proteins degrade over time, and more time has elapsed at the later time point. Moreover, between the 6 and 10 month time points, age-related tissue dysfunction is already evident in the ovary. For example, in 6-9 month old mice, there is already a deterioration of chromosome cohesion in the egg which results in increased interkinetochore distances (*41*), and by 10 months, there are multinucleated giant cells present in the ovarian stroma which is consistent with chronic inflammation (*20*). Thus, our results suggest that important shifts in the proteome occur during mid to advanced reproductive and may be another early feature of ovarian aging. Whether the LLPs at the 6 month time point serve as a protective mechanism in maintaining gamete quality or whether they contribute to decreased quality associated with reproductive aging is an intriguing dichotomy which will require further investigation.

A small subset of tubulins and histones persisted throughout the entire 10-month chase period, indicating that their replacement is exceptionally slow. LLPs which were present at both time points and persisted to at least 10 months may have important roles in the aging process. Interestingly, Tubb5 and Tubb4a have high homology to primate-specific Tubb8, and Tubb8 mutations in women are associated with meiosis I arrest in oocytes and infertility (*42, 43*). Thus, perturbation of these particular proteins by virtue of their long-lived nature may be associated with impaired function and poor reproductive outcomes, and these possibilities warrant future investigation. We noted that LLPs identified at 10 months were not always identified as long-lived at 6 months. This is a common limitation of mass spectrometry-based proteomics where each sample is prepared and run individually, which introduces variability between biological replicates, especially with respect to low abundant proteins. To compensate for this known and inherent variability, we applied stringent filtering criteria where we required long-lived peptides to be identified in an independent MS scan which provided us peptides of highest confidence.

By isolating fully grown oocytes from the ovary, we were able to determine the long-lived proteome of a purified germ cell population across the reproductive lifespan. Although we identified certain histone proteins as long lived, their relative fractional abundance was much lower than in the brain, a tissue which also contains post-mitotic cells (*14, 15*). However, histone-variant exchange occurs continuously during mouse oogenesis and is required for both transcriptional regulation and de novo DNA methylation (*44*). Thus, turnover and exchange of histones is likely more dynamic than previously assumed in terminally differentiated or post-mitotic cells, and our findings are consistent with this in the oocyte. Myosin and actin were also identified as LLPs with relatively high fractional abundance indicating exceptional longevity beyond 6-months. These proteins play numerous roles in oocyte maturation, fertilization, and egg activation, including nuclear positioning, spindle rotation and anchoring, chromosome segregation, cytokinesis, cortical granule exocytosis, and cytoplasmic flow (*19, 45-49*). Defects in many of these processes have been reported with advanced reproductive age, but whether long-lived pools of actin and myosins contribute to this etiology remains to be elucidated (*50*). Interestingly, F-actin stabilization restricts chromosome segregation errors due to cohesion loss which increase with age, so long lived pools of actin may confer a beneficial effect and protect against aneuploidy (*49*). The molecular mechanism(s) governing the longevity of the specific identified proteins in oocytes and ovaries as well as their relationship to the age-related decline in fertility and ovarian function require further investigation.

Mitochondrial proteins were the predominant LLPs in isolated oocytes across the reproductive lifespan, and it is plausible that ^{15}N cytoplasmic hotspots in oocytes that were observed in MIMS may correspond to mitochondria. Various aspects of mitochondrial dysfunction have been long-implicated in the age-dependent decline in gamete quality, with an age-dependent decrease in the number of mitochondria, an increase in abnormal morphology, and altered subcellular distribution (*51*). Moreover, mtDNA copy

number decreases with age, whereas mtDNA mutations increase (*52, 53*). Finally, the functional capacity of mitochondria decreases with age with decreased membrane potential, increased reactive oxygen species, increased oxidative stress, and decrease energy output (*54*). Although it is possible that oocyte long lived mitochondrial proteins deteriorate with age and contribute to mitochondrial dysfunction, a different model is emerging for these proteins. Mitochondrial proteins are exceptionally long lived in tissues containing long-lived terminally differentiated cells and have now been documented in the brain (neurons), heart (cardiac myocytes), and the ovary (oocytes) (*13*). These mitochondrial LLPs are primarily localized to the cristae invaginations, which are throughout to serve as long-term stable ultrastructure within mitochondria. This strategic enrichment is hypothesized to serve as a lifelong structural pillar of mitochondria to support and maintain these organelles over long time frames (*16*). Although mitochondrial LLPs persist for at least 6 months in oocyte, the majority were undetectable by 10 months. Thus, it is tempting to speculate that a stable pool of mitochondrial LLPs provides structural support for the maintenance of mitochondrial structure and function early during the reproductive lifespan. However, turnover of mitochondrial LLPs later in the reproductive lifespan may serve as a biological timer of aging. Because mitochondria are maternally inherited, these mitochondrial LLPs formed during fetal development of the mother are likely transferred to the embryo and impact subsequent generations (*55*). Further investigation into the role of long-lived mitochondrial proteome in oocytes is necessary to understand their life-long contribution to reproductive health and fertility outcomes.

Acknowledgements

Funding: This research was supported by NICHD R21HD098498 to JNS and FED, NIA R21AG072343 to JNS. EKBW was supported by the NINDS F32 NS106812 and NINDS K99NS126639.

Author contributions: Conceptualization: EKBW, JNS, FED; Methodology: JSN, FED, EKBW, KMV, LTZ, SE, CG, FG, MS, Investigation: EKBW, KMV, LTZ, SE; Visualization: EKBW, KMV; Funding acquisition: JNS, FED; Project administration: JNS, FED; Supervision: JNS, FED; Writing – original draft: EKBW, KMV, JNS, FED; Writing – review & editing: all authors.

Competing interests: The authors declare no competing interests.

Data and materials availability: All data generated or analyzed during this study are included in the manuscript and supporting files. RAW MS data has also been deposited at MassIVE under the accession number MSV000092217

Supplementary Materials

Materials and Methods

Figs. S1 to S3

Tables S1 and S2

Table S1. Summary of proteins identified in 6- and 10-month chase ovaries.

Table S2. Summary of proteins identified in 6 and 10-month chase oocytes.

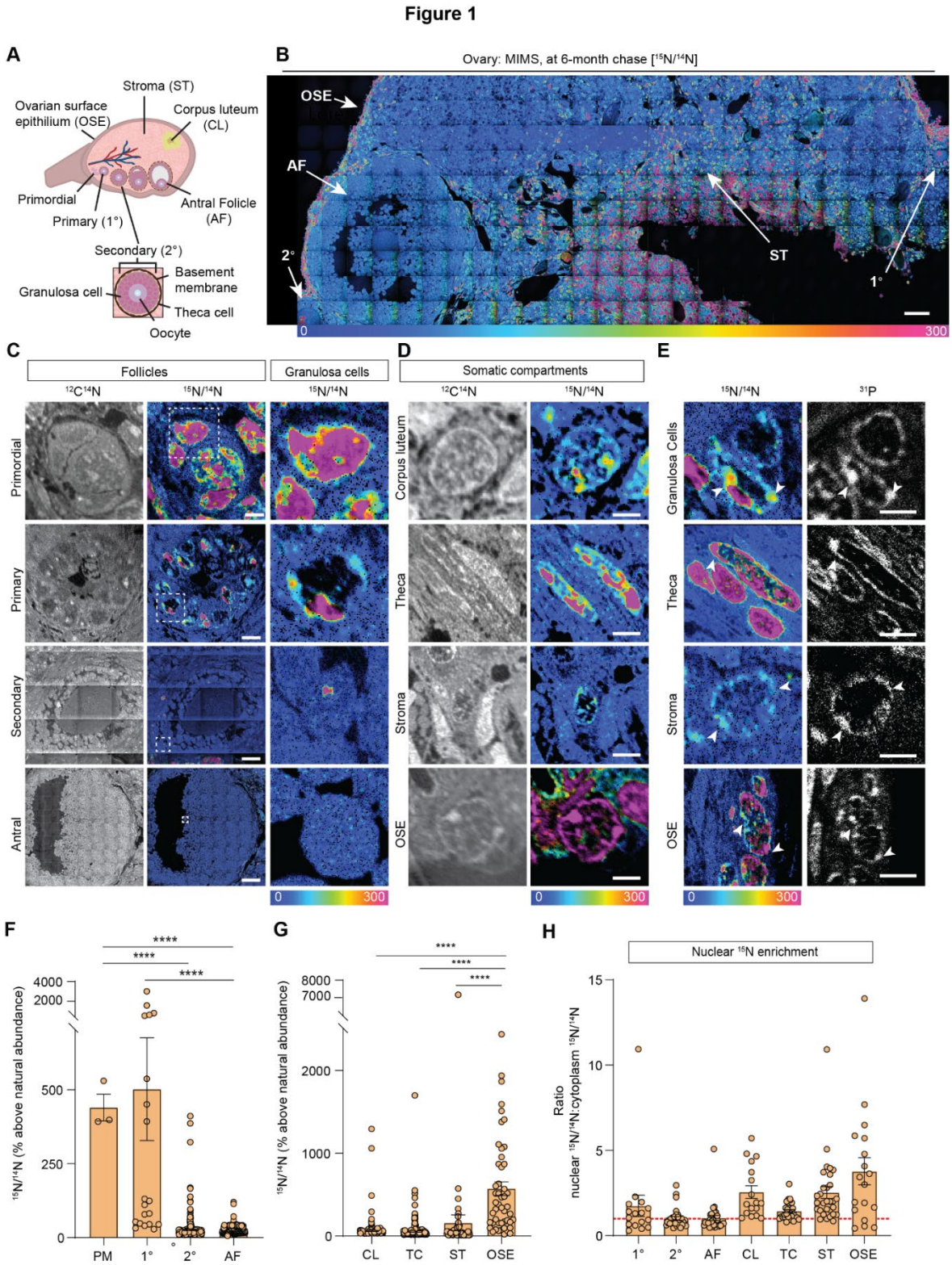

Fig. 1: MIMS analysis of cells and structures across ovarian tissue sections. (A) Diagram depicting and defining structures of the mammalian ovary. **(B)** Representative hue saturation intensity (HSI) mosaic from an ovary of a ^{15}N labeled mouse (6 months old). Localization and abundance of ^{15}N varied depending on cell type. HSI scale was set to 0% (natural $^{15}N/^{14}N$ ratio) to 300% (above the natural ratio). Scale bar = 60 µm. **(C)** High abundance of ^{15}N is seen in early-stage follicles, specifically within granulosa cells. **(D)** Representative images of somatic cells show differences in ^{15}N labeling. **(E)** Intracellular abundance

of ^{15}N is colocalized with ^{31}P abundance across all cell types. **(F)** Differences in $^{15}N/^{14}N$ ratios reveal granulosa cells of early-stage follicles have greater ^{15}N abundance than later stages. **(G)** Among somatic cells, quantitative analysis shows a greater abundance of ^{15}N at the ovarian surface epithelium. **(H)** Ratio analysis show abundance of ^{15}N localized in nuclear regions of cells. A hypothetical ratio of one, denoted as a red dash line, signifies no difference in ^{15}N abundance between cytoplasmic and nuclear regions.

Abbreviations: PM (primordial follicle), 1° (primary follicle), 2° (secondary follicle), AF (antral follicle), CL (corpus luteum), TC (theca cell), ST (stroma), and OSE (ovarian surface epithelium). HSI scale for all images was set to 0%-300% (above natural abundance). Data are shown as mean±SEM. Statistical analysis was performed using a one-way ANOVA. Asterisk denotes statistical significance (* $p \leq .05$; ** $p \leq .01$; *** $p \leq .001$; **** $p \leq .0001$). Scale bar = (B): 50 µm; (C): 3 µm (PR), 6 µm (1°), 30 µm (2°), 75 µm (AF); (D): 2.5 µm (CL), 2.5 µm (TC), 5 µm (ST), 2.5 µm (OSE); (E): 3 µm (GC), 3 µm (TC), 2.5 µm (ST), 6 µm (OSE).

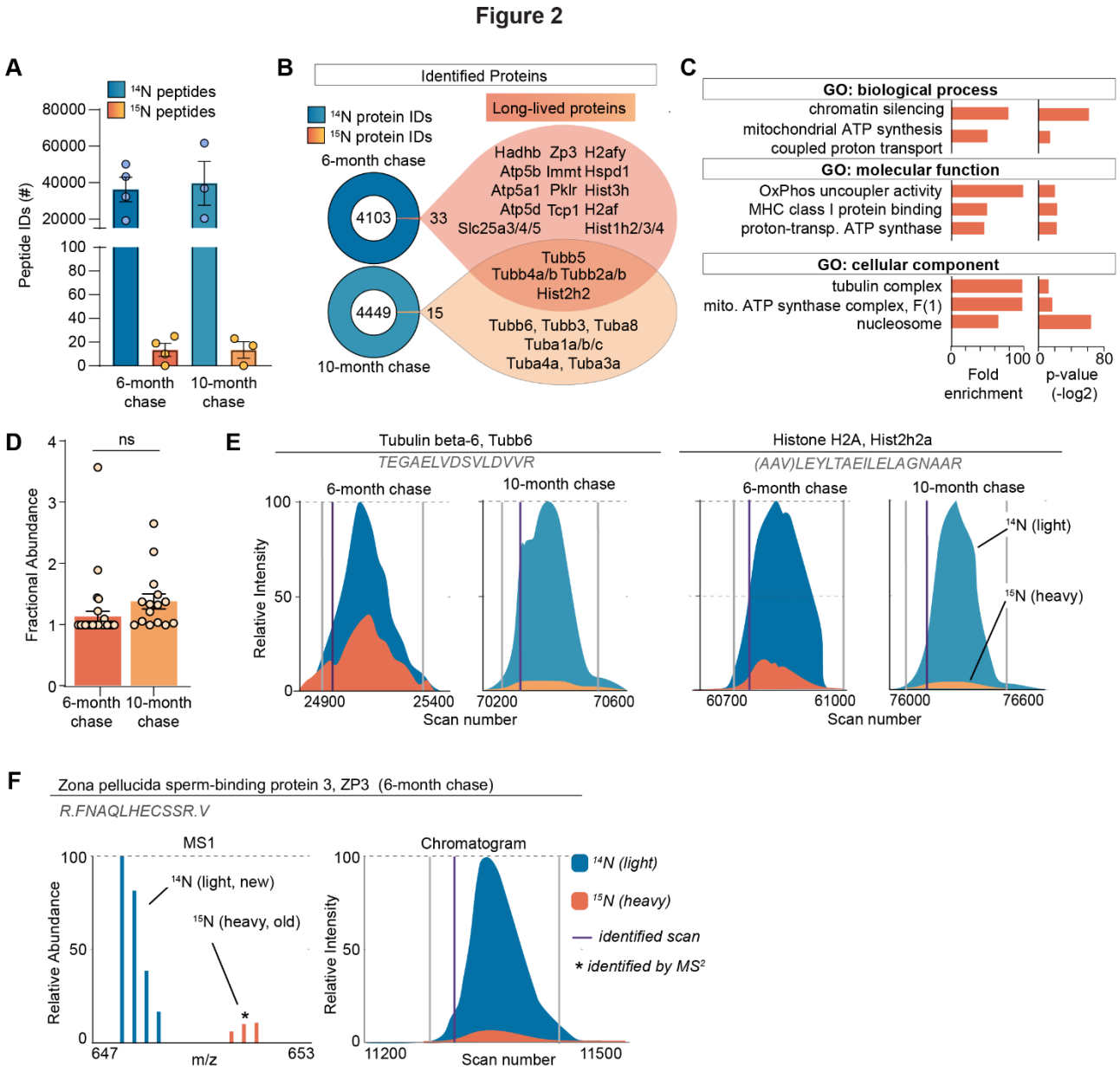

Fig. 2. Long-lived proteome in mammalian ovaries. **(A)** Summary of peptide identification at 6 and 10-month chase points, blue graphs indicate ^{14}N peptide IDs, orange/yellow graphs indicate ^{15}N peptide IDs. **(B)** Summary of protein identification at each time point, with a list of proteins identified as long-lived in orange. **(C)** GO analysis of the LLPs identified in ovaries at 6-months chase revealed that terms related to chromatin, nucleosome, tubulins, and mitochondria are significantly enriched. **(D)** Fractional abundance of LLPs identified at 6 and 10-month chase. **(E)** Annotated representative chromatograms of two representative proteins that persist through both 6- and 10-montch chase, illustrating the decreasing ^{15}N-signal over time. blue - 14N (new), orange 15N (old), purple line: identified scan. (**F**) Annotated representative raw MS1 scan of Zona Pellucida protein 3 (ZP3). Mean ± SEM; 3-4 biological replicate per timepoint, ns – not significant by Student's t-test.

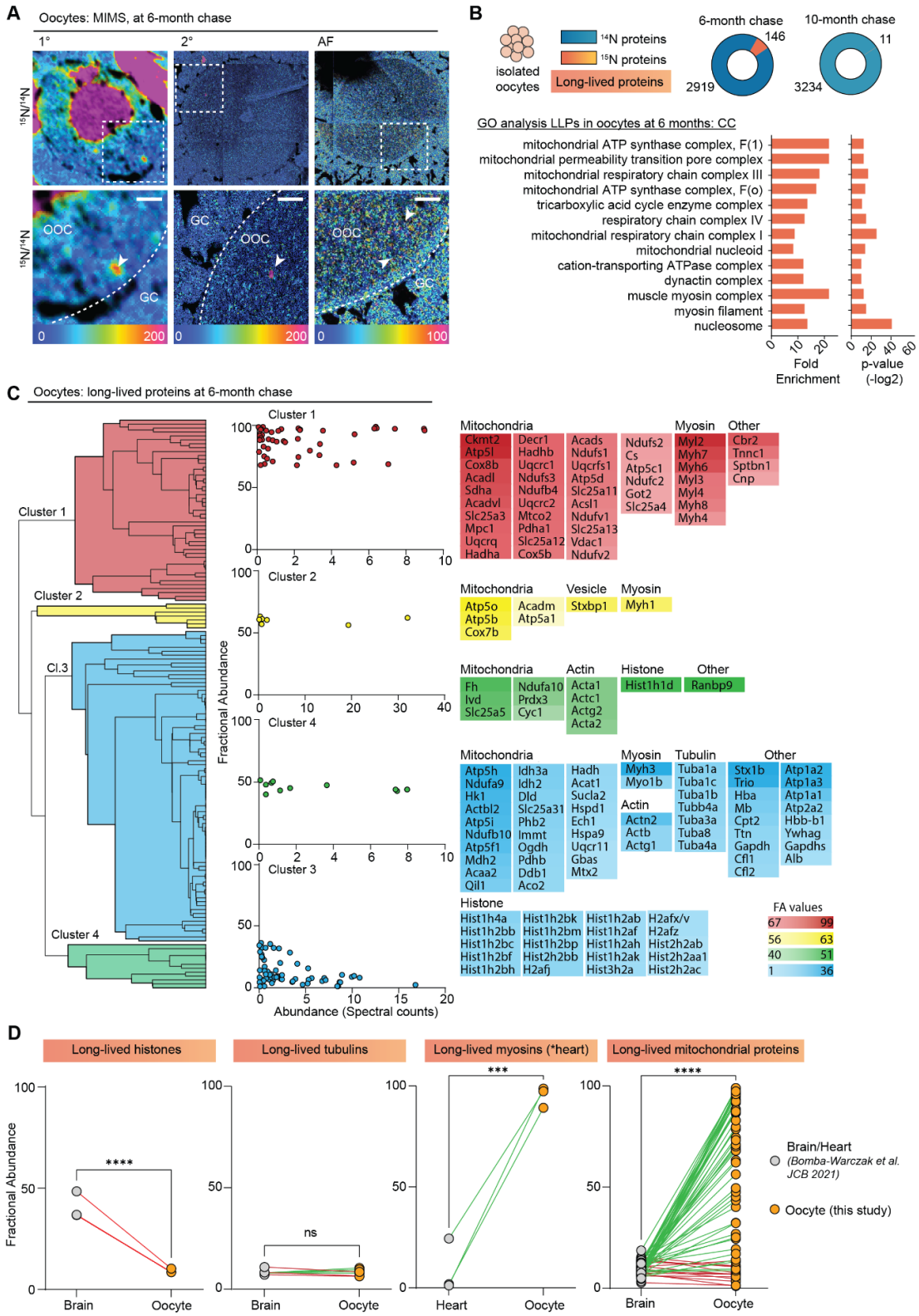

Fig 3. Exceptional longevity of nuclear, cytoskeletal, and mitochondrial proteins in mouse oocytes. **(A)** MIMS analysis reveals high abundance of ^{15}N in nuclei and throughout the cytoplasm of oocytes. **(B)** Purified oocyte population was harvested from pulse-chased mice and analyzed using gel-LC-MS/MS.

Charts illustrate the number of proteins identified at each timepoint (blue) along with long-lived proteins (orange). GO analysis of the LLPs identified in oocytes at 6-months chase revealed an enrichment for terms related to nucleosome, myosins, and mitochondria. **(C)** Hierarchical cluster analysis of fractional abundance of LLPs identified in oocytes. **(D)** Direct comparison of fractional abundances of proteins previously identified as long-lived and LLPs in oocytes. Mean ± SEM; Oocytes collected from 4-7 females per time-point, *** p-value <.001, **** p-value < .0001 by Kruskal-Wallis ANOVA with Tukey's multiple comparisons test. Scale bar = 4 µm.

Supplementary Figure 1

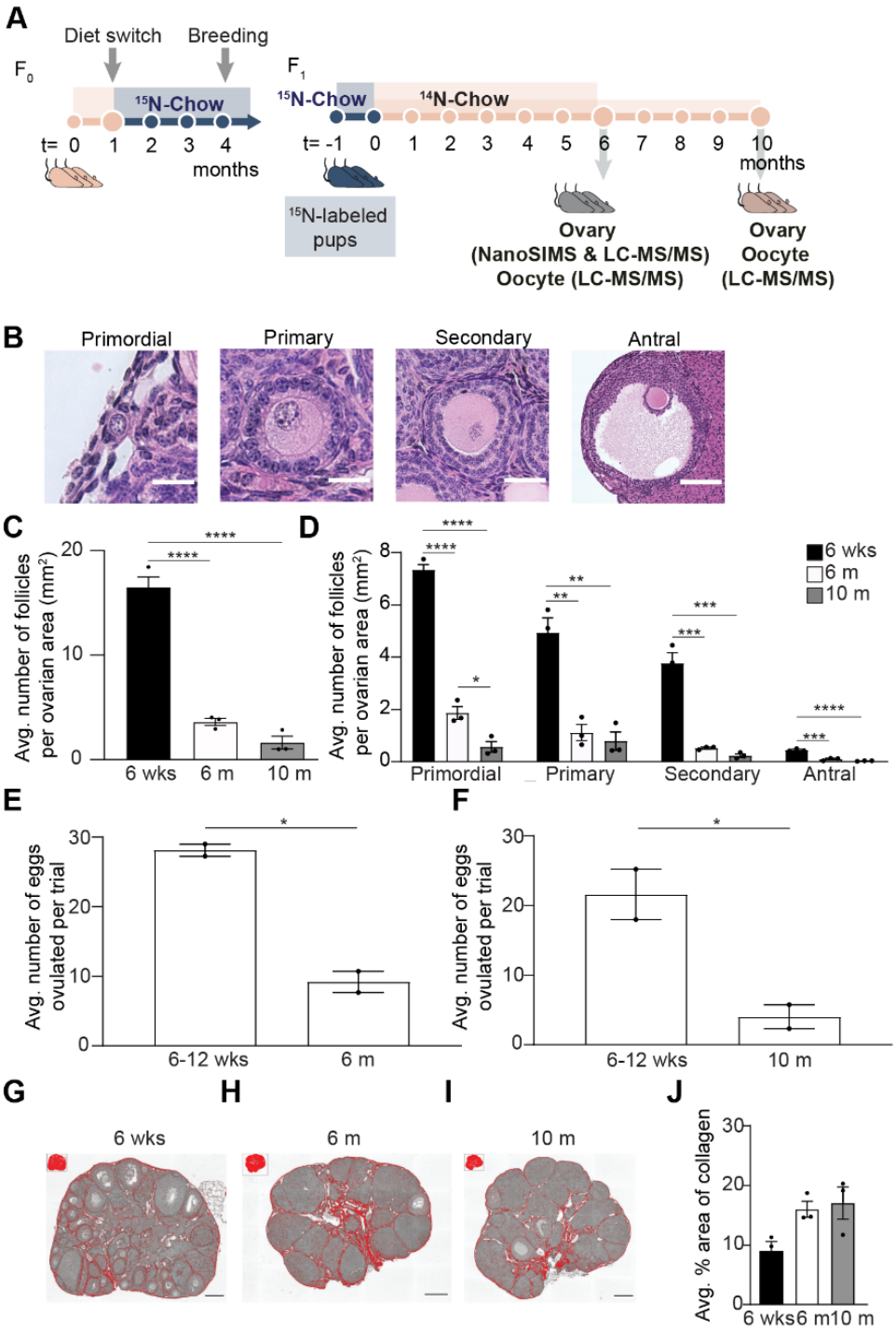

Fig. S1: Multi-generational whole animal pulse-chase labeling design along the reproductive aging continuum. (A) Wild-type female FVB mice (n=3) were fed a ^{15}N-diet for 13 weeks and were maintained on a ^{15}N-labeled diet through breeding, pregnancy, and weaning to produce ^{15}N-labeled pups. Labeled

pups were sacrificed after switching over to a ^{14}N-diet for a chase period of 6- or 10-months. Ovaries and oocytes were designated for NanoSIMS, or liquid-chromatography/mass spectrometry. Female FVB mice experience age-associated changes in ovarian reserve, ovarian microenvironment, and gamete quality. **(B)** Representative images of each follicle class from mice of 6 weeks old and 6 months old. **(C)** Average follicle number per area of ovarian section from mice of the following ages: 6 weeks, 6 months, and 10 months (N= 3 mice per age cohort). **(D)** Graph represents average number of follicles within each follicle class per area of ovarian section for mice ages 6 weeks, 6 months, and 10 months. (**E**) Comparison of average number of eggs ovulated per trial for mice at 6-12 wks, 6 months, and (**F**) 10 months. The data points represent the average number of eggs collected per mouse from two independent trials. In each trial, oviducts from 3-4 mice were pooled per age group. Representative processed color threshold images of PSR-stained ovarian tissue sections from mice **(G)** 6 weeks old, **(H)** 6 months old, and **(I)** 10 months old**. (J)** Graph comparing the average percent area of PSR-positive staining per ovarian section (pixels/μm^2). Data are shown as mean ± SEM. Statistical analysis was performed using a one-way ANOVA. Asterisk denotes statistical significance (* $p \leq .05$; ** $p \leq .01$; *** $p \leq .001$; **** $p \leq .0001$). Scale bar for images of (B) primordial, primary, secondary, and antral follicles are 20 µm, 40 µm, and 140 µm, respectively. Scale bars in (G-I) are 180 µm.

Supplementary Figure 2

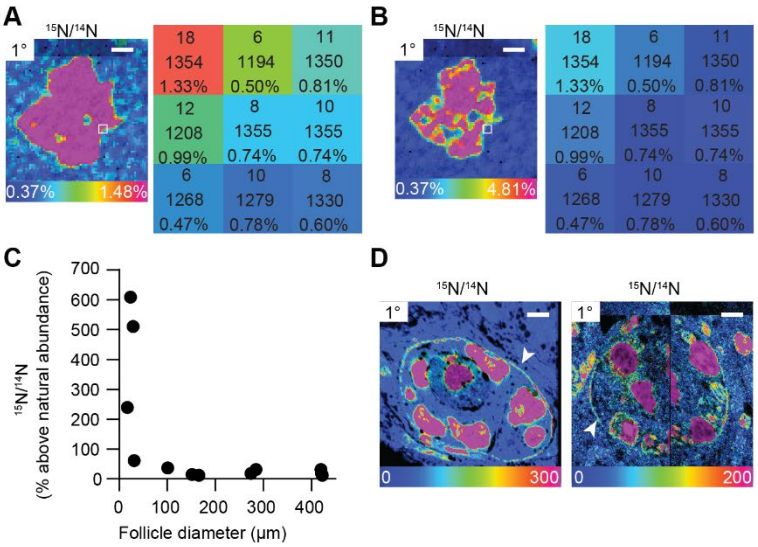

<u>Fig. S2:</u> Multi-isotope imaging mass spectrometry (MIMs) uncovers structures enriched with ^{15}N. (A) Hue saturation intensity image maps ^{15}N/^{14}N ratio across nuclear region of a primary follicle. Using a rainbow scale, blue is set to the natural ratio of ^{15}N (0.37%) and overabundance is set to 1.48% (or 300% above the natural ratio). Each pixel provides quantitative information. The numbers in each pixel represent the number of ^{15}N ions, ^{14}N ions, and the ^{15}N/^{14}N ratio, respectively. **(B)** Changes to the rainbow scale can be used to emphasize regional ratio differences and change the visual representation of the data. Visual changes to HSI images due to different scales, does not change the quantitative data behind each pixel. **(C)** Total ^{15}N abundance of each follicle plotted by follicle diameter shows smaller follicles containing high abundance of ^{15}N. **(D)** HSI images reveal high ^{15}N abundance concentrated at the basement membrane of early-stage follicles. Scale bar (panel A-B) =2.5 µm, (D) left= 4.0 µm, (D) right = 4.5 µm.

Supplementary Figure 3

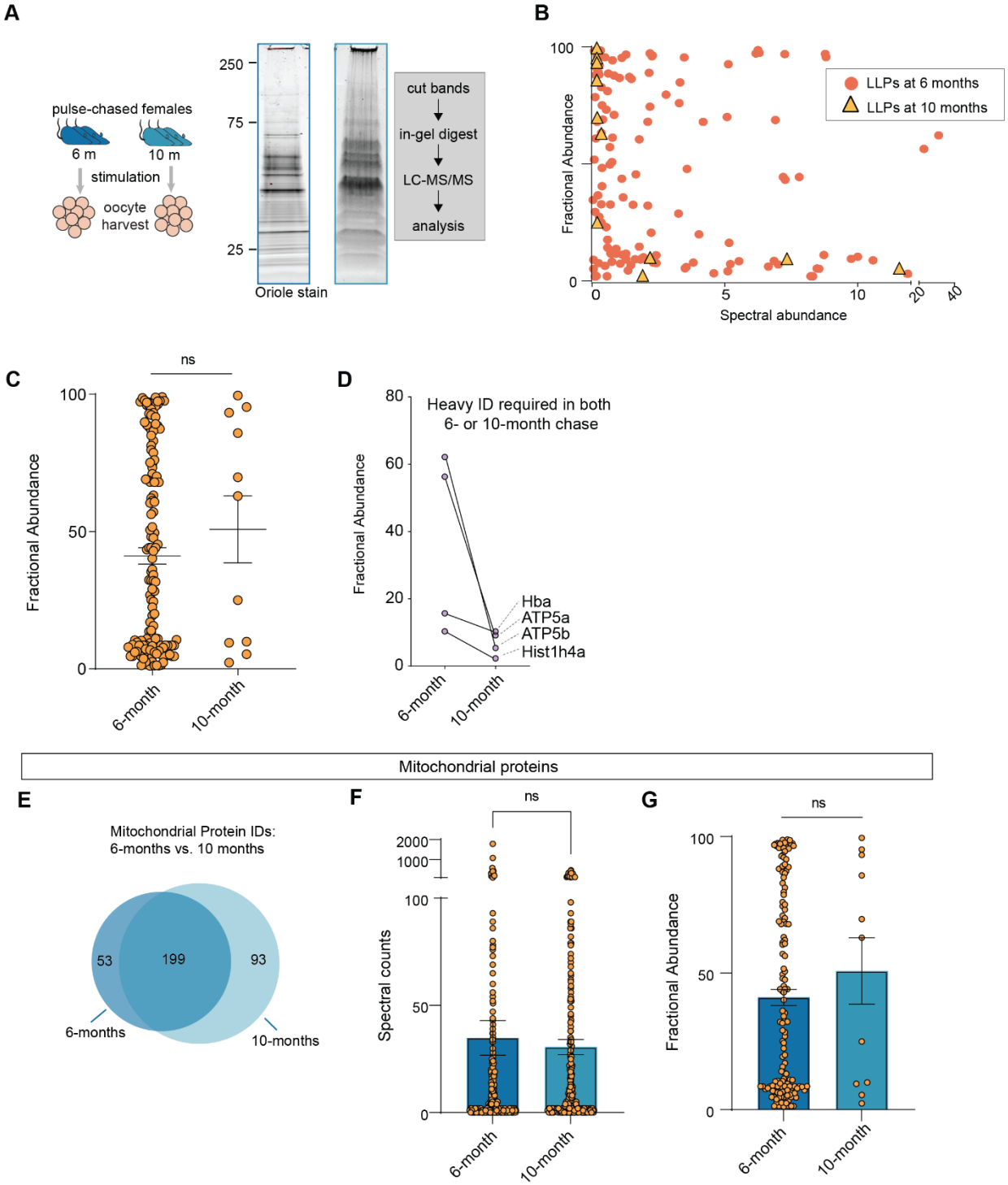

Fig. S3: Long-lived proteins at 6- and 10-months chase points in oocytes. (A) Experimental scheme to identify and measure LLPs mouse oocyte. **(B-C)** Fractional abundance of each identified LLPs at both 6 months and 10 months as compared to the spectral abundance for each LLPs. **(D)** Plots showing decrease in FA values for same proteins identified as LLPs at 6 and 10-month chase. (E) Venn diagram illustrating the overlap of mitochondrial proteins identified at 6 and 10-month time points (F) Spectral counts of mitochondrial proteins as well as the (G) fractional abundance of each identified mito-LLPs at both 6 months and 10 months, illustrating that even though there are no significant difference in spectral counts

424 at each timepoint, the number of quantified proteins decreased dramatically between 6 and 10 months of
425 chase.

426 Materials and Methods
427
428 *Animals*
429 Mice of the FVB strain were obtained from Jackson Laboratory (Bar Harbor, ME). For the whole animal
430 isotope pulse-chase labeling strategy, female (5 weeks old) and male mice (10 weeks old) mice were
431 obtained. To validate the biological relevance of our chase period, reproductive aging parameters were
432 evaluated in unlabeled female mice at 6 weeks, 6 months, and 10 months of age. Retired female FVB
433 mouse breeders were obtained at 15 weeks of age and aged out to 6 months and 10 months. Mice were
434 acclimated in the vivarium upon arrival for at least two weeks prior to experimental use. All mice were
435 housed at Northwestern University's Center for Comparative Medicine under constant temperature,
436 humidity, and light (14 hours light/10 hours dark). Mice were fed and provided with water *ad libitum*. All
437 animal care and experimental protocols in this study were conducted under the guidelines set by the NIH
438 Guide for the Care and Use of Laboratory Animals handbook, and the animal protocol was approved by
439 the Animal Care and Use Committee of Northwestern University.
440
441 *Pulse-chase labeling strategy*
442 Mice were metabolically labeled using a two-generation metabolic pulse-chase labeling strategy as
443 previously described (*13*). Briefly, three female FVB mice were fed a spirulina ^{15}N-containg chow for the
444 duration of the study (initial labeling, breeding, pregnancy, and weaning) (Cambridge Isotope
445 Laboratories, Inc., Tewksbury, MA). After 13 weeks of being on a ^{15}N diet, these labeled females were
446 co-housed with unlabeled males for 5 days to allow a complete estrous cycle for breeding. Pregnant
447 females were housed separately to allow for accurate dating of litter births. All females were allowed to
448 breed a total of 3-5 times to obtain sufficient pups for the chase period. The pulse period was defined as
449 the timespan between gestation and weaning of pups. Thus, pups conceived from labeled females had
450 nitrogen-containing molecules and proteins labeled with ^{15}N. At 22 days old, pups were weaned and fed
451 a ^{14}N diet *ad libitum*. Pups were maintained on a ^{14}N diet (chase) until they reached 7 and 11 months of
452 age at which point tissues were harvested for downstream analyses. This animal labeling strategy
453 generated 19 female pups. For ovary studies, 4 mice were used at 6 months post-chase and 4 mice at 10
454 months post-chase. One ovary per mouse was used for MIMS, and the contralateral ovary was used for
455 LC-MS/MS. For oocyte studies, 4 mice were hyperstimulated at 6 months post-chase and 7 mice at 10
456 months post-chase. A total of 104 and 45 oocytes were collected at 6 months and 10 months post-chase,
457 respectively, and these samples were used for LC-MS/MS.
458
459 *Ovary and oocyte collection*
460 Ovaries were harvested and placed in a dish containing pre-warmed Leibovitz's medium (L15) (Life
461 Technologies Corporation, Grand Island, NY) supplemented with 3 mg/mL polyvinylpyrrolidone (PVP)
462 (Sigma-Aldrich, St. Louis, MO), 0.5% penicillin-streptomycin (Life Technologies) (L15-PVP). Ovaries
463 were either processed as described below for downstream analyses or used to isolate oocytes. Ovaries
464 used to assess reproductive aging parameters were fixed for histological analysis in Modified Davidson's
465 (Electron Microscopy Sciences, Hatfield, PA) at room temperature for 2-4 hours with agitation and
466 overnight at 4°C. Ovaries used for MIMS were cut in half and fixed in 2% glutaraldehyde (Electron
467 Microscopy Sciences, Hatfield, PA) and embedded in LR white (EMS). Ovaries used for LC-MS/MS
468 were snap frozen and stored at -80°C until use.
469
470 To maximize the yield of a synchronized population of fully grown oocytes for LC-MS/MS, mice were
471 hyperstimulated with an intraperitoneal injection of 5 IU pregnant mare serum gonadotropin (PMSG)
472 (Prospec Bio, East Brunswick, N). Ovaries were harvested 44-48 hours post-PMSG injection and placed
473 in L15-PVP supplemented with 0.025% milrinone to maintain oocyte meiotic arrest (Sigma-Aldrich, St.
474 Louis, MO).

Cumulus-oocyte-complexes (COCs) were released by puncturing antral follicles with insulin syringes. Oocytes were mechanically denuded from cumulus cells using a 75 µm stripper tip and washed thoroughly in L15/PVP/PS before being snap frozen. For analysis of ovulated eggs, mice were hyperstimulated as described above with PMSG followed by superovulation induction 44-46 hours later with an intraperitoneal injection of 5 IU human chorionic gonadotropin (hCG)(Sigma, St. Louis, MO). COCs were then collected from the oviducts of each mice 14-16 hours post-hCG injection, and the number of ovulated eggs were counted.

Ovarian follicle counts and histological analysis

The decline in the number of ovarian follicles is a hallmark of reproductive aging (*1*). Therefore, we evaluated follicle counts in histological sections of ovaries as done previously (*9*). In brief, fixed ovaries were washed three times with 70% ethanol and processed, dehydrated, and paraffin embedded using an automated tissue processor (Leica Biosystems, Buffalo Grove, IL). After embedding, ovaries were serial sectioned with every 5th tissue section stained with hematoxylin and eosin (H&E). All H&E-stained tissue sections were digitally scanned at the University of Washington's Histology and Imaging Core using Hamamatsu-HT imaging system (Hamamatsu Photonics, Hamamatsu City, Japan) at 20X magnification. Scanned images were uploaded and visualized using the NDP.view2 software (Hamamatsu Photonics, Hamamatsu City, Japan). Follicles were classified and counted in every 5th tissue section. Follicles were classified by stage (primordial, primary, secondary, and antral) according to established criteria (*9*). Primordial follicles were comprised of an incomplete layer of squamous granulosa cells, while primary follicles contained a complete layer of cuboidal granulosa cells. Secondary follicles contained two or more layers of cuboidal granulosa cells. Antral follicles had more than eight layers of granulosa cells with the presence of an antrum, or fluid-filled cavity. All primordial and primary follicles were counted regardless of whether the oocyte's nucleus was visible. Secondary and antral follicles were counted only if the nucleus was visible to avoid double counting. Only healthy follicles were included in the final counts. Atretic follicles containing abnormally shaped oocytes with dark, pyknotic granulosa cells were excluded. The average number of follicles per area of ovarian section was calculated and used to compare counts between each age cohort.

Ovarian fibrosis, characterized by excess collagen, is another hallmark of reproductive aging (*19*). We evaluated fibrosis in ovaries by Picrosirius Red (PSR), a histological stain which detects collagen I and III (*19*). Ovarian tissue sections were deparaffinized in Citrisolv (Fisher Scientific, Pittsburgh, PA) and rehydrated in 100%, 70%, and 30% ethanol baths. Slides were submerged in PSR staining solution composed of Sirius Red F3BA (Direct Red 80, C.I. 357.82, Sigma-Aldrich, St. Louis, MO) and picric acid (Sigma-Aldrich, St. Louis, MO) at 0.1% w/v for 40 minutes at room temperature. The slides were then incubated in acidified water made of 0.05 M hydrochloric acid (Fisher Scientific) for 90 seconds. Tissue sections were dehydrated in 100% ethanol baths, three times for 30-second incubations. After dehydration, slides were immersed in Citrisolv for five minutes and mounted with Cytoseal XYL (Fisher Scientific). PSR stained sections were then imaged with an EVOS FL Auto Imaging system (Thermo Fisher, Waltham, MA) using a 20X objective. Scans of whole ovarian tissue sections were performed to quantify the area of positive PSR staining using a threshold feature on ImageJ as previously described (Briley et. 2016). PSR positive staining was analyzed on two different ovarian tissue sections for three mice within each age cohort: 6 weeks, 6 months, and 10 months. Results were averaged to obtain average percent area of collagen.

Multi-isotope imaging mass spectrometry (MIMS) and data processing

Fixed LR white-embedded ovaries were sectioned to 0.5 microns and mounted on silicon wafers. At the Brigham and Women's Hospital Center for NanoImaging, a NanoSims 50L (CAMECA Instruments Inc.,

524 Madison, WI) instrument was tuned to simultaneously measure $^{12}C^{14}N^-$, $^{12}C^{15}N^-$, and $^{31}P^-$ secondary ions
525 as described previously for imaging of a wide range of mouse and human tissues (*56*). Quantitative $^{12}C^{14}N$
526 images were used for histological representation of stereotypical ovarian structures and associated cell
527 types. ^{31}P images provided additional histological detail and were used for identification of nuclei due to
528 the high phosphorus content of chromatin (*29*). Quantitative mass images for $^{12}C^{14}N$ and $^{12}C^{15}N$ were
529 used to generate quantitative ^{15}N:^{14}N ratio images. For imaging of swathes of the tissue section, images
530 were acquired in chain analysis mode of sequential adjacent fields (dimensions of 45 µm x 45 µm or 50
531 µm x 50 µm). Sequential tiles were stitched together to make mosaic images for visualizing large sections
532 of the ovary (**Fig. 1B**). Some features were then imaged at higher resolution with smaller field sizes. All
533 images were processed and further analyzed using the most recent version of the OpenMIMS 2.0 plugin
534 (https://github.com/BWHCNI/OpenMIMS) to ImageJ (*57*). ^{15}N-labeling was visualized by a hue
535 saturation intensity (HSI) transformation of the $^{12}C^{15}N$/ $^{12}C^{14}N$ ratio. The color scale of HSI images is set
536 such that the lower blue bound of the scale is at the ^{15}N natural abundance of 0.37% (expressed as 0 %
537 above background). The upper magenta bound of the scale is set to reveal labeling differences. The
538 quantitative isotope ratio measurements that form the basis for the images and that are used for statistical
539 analyses are not affected by scaling changes that modify the visual appearance of the images (**fig. S2 A-**
540 **B).** A combination of ^{14}N and ^{31}P images were used to manually select regions of interest within each
541 ovarian section (e.g. individual cells or subcellular structures). Structures and cell types were identified
542 based on morphology and their anatomic location. Cells that were not identifiable or were not visualized
543 due to low ion counts were excluded from the analysis. Typical reasons for difficult identifying cells
544 include sectioning artifacts (cracks, wrinkles) or certain cells that were located at the juncture between
545 adjacent imaging fields, where there is often lower yield of secondary ions. This edge effect is seen to
546 variable degrees in the mosaic images as dark regions at the periphery of an imaging field. All quantitative
547 data for ^{15}N-labeling was presented as the $^{15}N/^{14}N$ ratio (percentage above natural abundance).
548
549 *Mass Spectrometry (MS) sample preparation: ovaries*
550 Isolated ovaries were homogenized directly in 6M guanidine hydrochloride solution using bead-based
551 Precellys 24 homogenizer, followed by processing with ProteaseMAX according to manufacturer's
552 protocol. Samples were reduced with 5 mM Tris(2-carboxyethyl)phosphine (TCEP; vortex 1 hr at RT)
553 alkylated in the dark with 10 mM iodoacetamide (IAA; 20 min), diluted with 50 mM ABC and quenched
554 with 25 mM TCEP. Samples were digested with sequencing grade modified trypsin overnight at 37°C
555 with shaking, spun down (15,000 × g for 15 min at RT), placed in a new tube and acidified with TFA to
556 a final concentration of 0.1%. A total of 100 µg of digested and acidified sample was fractionated using
557 High pH Reversed-Phase Peptide Fractionation Kit (Pierce, Cat# 84868). Fractions were step eluted in
558 300 µL buffer of increasing acetonitrile (ACN) concentrations with decreasing concentration of
559 Triethylamine (0.1%) as per manufacturer. Samples were dried down with vacuum centrifugation for
560 future MS analysis.
561
562 *MS sample preparation: GeLC/MS on oocytes*
563 Isolated oocytes were lysed directly in RIPA buffer, mixed with 6X SDS sample buffer, boiled for 5
564 minutes, and separated by SDS-PAGE using 10% Tris-glycine gels (Thermo Scientific, Cat#
565 XV00100PK20). Gels were stained using Oriole fluorescent gel stain solution, scanned using Bio-rad
566 Chemidoc XRS system, and cut into sections, chopped into 1mm x 1 mm cubes, and processed for in-gel
567 digestion. The gel separating oocytes collected at t=6 months was cut into 36 individual pieces, whereas
568 the gel separating oocytes collected at t=10 months was cut into 24 pieces. Gel pieces were incubated in
569 10 mM TCEP (in 50 mM ABC; 1 hr at 37 °C). Liquid was replaced by 50 mM IAA (in 50 mM ABC; 45
570 min at RT in dark), followed by 50 mM TCEP (in 50 mM ABC; 30 min at RT). Gel pieces were washed
571 with 50 mM ABC (3x) and digested with sequencing grade modified trypsin (1 µg in 50 mM ABC,
572 overnight at 37 °C, with shaking). The following day, supernatant was collected into new tube and the gel

573 piece were subjected to three rounds of incubations with 50% ACN and 5% FA solution (30 min at RT,
574 with shaking). Supernatant was collected after each incubation, combined, and dried down with vacuum
575 centrifugation. Samples were re-suspended in 0.5% TFA, desalted with Pierce C18 spin columns (Thermo
576 Scientific, Cat# 89873) per manufacturer's instructions, and dried down with vacuum centrifugation for
577 future MS analysis.
578
579 *MS analysis*
580 Dried samples were re-suspended in 20 µL Buffer A (94.875% H2O with 5% ACN and 0.125% FA) and
581 three micrograms, as determined by microBCA assay (Thermo Scientific, Cat# 23235) of each fraction or
582 sample were loaded via auto-sampler with either Thermo EASY nLC 100 UPLC or UltiMate 3000 HPLC
583 pump, onto a vented Pepmap 100, 75um x 2 cm, nanoViper trap column coupled to a nanoViper analytical
584 column (Thermo Scientific) with stainless steel emitter tip assembled on the Nanospray Flex Ion Source
585 with a spray voltage of 2000 V. A coupled Orbitrap Fusion was used to generate MS data. Buffer A
586 contained 94.785% H_2O with 5% ACN and 0.125% FA, and buffer B contained 99.875 ACN with 0.125%
587 FA. MS parameters were as follows: Ion transfer tube temp = 300 °C, Easy-IC internal mass calibration,
588 default charge state = 2 and cycle time = 3 s. Detector type set to Orbitrap, with 60K resolution, with wide
589 quad isolation, mass range = normal, scan range = 300-1500 m/z, max injection time = 50 ms, AGC target
590 = 200,000, microscans = 1, S-lens RF level = 60, without source fragmentation, and datatype = positive
591 and centroid. MIPS was set as on, included charge states = 2-6 (reject unassigned). Dynamic exclusion
592 enabled with n = 1 for 30 s and 45 s exclusion duration at 10 ppm for high and low. Precursor selection
593 decision = most intense, top 20, isolation window = 1.6, scan range = auto normal, first mass = 110,
594 collision energy 30%, CID, Detector type = ion trap, OT resolution = 30K, IT scan rate = rapid, max
595 injection time = 75 ms, AGC target = 10,000, Q=0.25, inject ions for all available parallelizable time. For
596 ovary samples the chromatographic run was 4.5 hours per fraction, with the following profile of Buffer
597 B: 2% for 7 min, 2-7% for 1 min, 7-10% for 5 min, 10-25% for 160 min, 25-33% for 40 min, 33-50% for
598 7 min, 50-95% for 5 min, 95% for 15 min, then back to 2% for the remaining 30 min. For the GeLC/MS
599 oocyte samples, the chromatographic run was 75 min per gel section with the following profile of Buffer
600 B: 2-8% for 6 min, 8-24% for 10 min, 24-36% for 20 min, 36-55% for 10 min, 55-95% for 10 min, 95%
601 for 10 min, then back to 2% for remaining 9 min.
602
603 *MS Data Analysis and Quantification*
604 Protein identification/quantification and analysis were performed with Integrated Proteomics Pipeline -
605 IP2 (Integrated Proteomics Applications, Inc., San Diego, CA. http://www.integratedproteomics.com/)
606 using ProLuCID (*58, 59*), DTASelect2 (*60, 61*), Census and QuantCompare. Spectral raw files were
607 extracted into MS1, MS2 files using RawConverter 1.0.0.0 (http://fields.scripps.edu/downloads.php). The
608 tandem mass spectra were searched against mouse database (downloaded on 03-25-2014). Searched
609 spectra were matched to sequences using the ProLuCID/SEQUEST algorithm (ProLuCID version 3.1)
610 with 50 ppm peptide mass tolerance for precursor ions and 600 ppm for fragment ions. ProLuCID searches
611 included all fully and half-tryptic peptide candidates that fell within the mass tolerance window and had
612 with unlimited mis-cleavages. Carbamidomethylation (+57.02146 Da) of cysteine was considered as a
613 static modification. Peptide/spectrum matches (PSMs) were assessed in DTASelect2 using the cross-
614 correlation score (XCorr), and normalized difference in cross-correlation scores (DeltaCN). Each protein
615 identified was required to have a minimum of one peptide (-p1) of minimal length of six amino acid
616 residues. False discovery rate (FDR) was set to 1% at the protein level, for all experiments. Peptide
617 probabilities and FDR were calculated based on a target/decoy database containing the reversed sequences
618 of all the proteins appended to the target database (*62*). Each dataset was searched twice, once against
619 light (^{14}N) and then against heavy (^{15}N) protein databases, as described previously(*14*). In the light
620 searches, all of the amino acid residues were considered to contain only ^{14}N nitrogen, while in the heavy
621 searches, all the amino acid residues were considered to contain only ^{15}N nitrogen. After the results from

ProLuCID were filtered using DTASelect2, and the assembled search result file was used to obtain quantitative ratios between ^{14}N and ^{15}N using the software Census (*30, 63*).

Long-lived proteins were identified as previously described, with modifications (*14*). Briefly, in order for a protein to be considered as long-lived, the protein had to be identified in our heavy/light search by at least one long-lived peptide (^{15}N-peptide). Peptide ratio measurements were filtered in Census based on a correlation threshold, and only peptides with correlation coefficient above 0.5 were used for further analysis. For singleton analysis, we required the $^{14}N/^{15}N$ ratio to be greater than 5.0 and the threshold score to be greater than 0.5. Identified peptides were further filtered based on their average peptide enrichment (APE), which we set to 0.9, and peptide profile score, which was set to 0.8. Proteins were only identified as long-lived if they had more than three long-lived peptides that passed the above filtering (except for GeLC/MS experiments where one peptide was required). Fractional abundance were calculated according to the following formula: ^{14}N values: $FA = 100 - (100*(1/(1+AR)))$, where FA = fractional abundance and AR = area ratio.

Gene Ontology Analysis

GO analysis was performed using the Pantherdb (*64*). The "query" is defined as proteins identified as long-lived in the analyzed tissue (based on ^{14}N-peptide identification), and the reference is defined as all proteins identified in the same tissue analyzed (^{14}N and ^{15}N-peptide identification).

Statistical analysis

Statistical analyses were conducted using GraphPad Prism, version 9 (GraphPad Software, Inc.). A Student's t-test was performed for comparisons between two groups. For comparisons of more than two groups, a one-way ANOVA was used. A one sample t-test was used to compare $^{15}N/^{14}N$ ratios of cytoplasmic and nuclear regions to a hypothetical value of 1. Values >1 signified a cell had greater ^{15}N-labelling abundance in the nucleus compared to the cytoplasm. Values <1 represented cells with a lower ^{15}N-labelling abundance in the nucleus compared to the cytoplasm. Values equal to 1 represented a cell with a ^{15}N-labelling abundance that were equivalent in both nuclear and cytoplasmic regions. Data were considered significant with a p-value <.05 (* p-value <.05, ** p-value <.01, *** p-value <.001). Variability of groups was denoted as standard error of mean (SEM).

652 **Uncategorized References**

653 1. F. J. Broekmans, M. R. Soules, B. C. Fauser, Ovarian aging: mechanisms and clinical
654 consequences. *Endocrine reviews* **30**, 465-493 (2009).
655 2. J. Reefhuis, M. A. Honein, Maternal age and non-chromosomal birth defects, Atlanta--1968-2000:
656 teenager or thirty-something, who is at risk? *Birth defects research. Part A, Clinical and molecular*
657 *teratology* **70**, 572-579 (2004).
658 3. C. T. Mai *et al.*, Selected birth defects data from population-based birth defects surveillance
659 programs in the United States, 2006 to 2010: featuring trisomy conditions. *Birth defects research.*
660 *Part A, Clinical and molecular teratology* **97**, 709-725 (2013).
661 4. L. M. Hollier, K. J. Leveno, M. A. Kelly, M. C. DD, F. G. Cunningham, Maternal age and
662 malformations in singleton births. *Obstetrics and gynecology* **96**, 701-706 (2000).
663 5. J. A. Johnson, S. Tough, O. Society of, C. Gynaecologists of, Delayed child-bearing. *J Obstet*
664 *Gynaecol Can* **34**, 80-93 (2012).
665 6. E. Buyuk, E. Nejat, G. Neal-Perry, Determinants of female reproductive senescence: differential
666 roles for the ovary and the neuroendocrine axis. *Semin Reprod Med* **28**, 370-379 (2010).
667 7. M. V. Sauer, Reproduction at an advanced maternal age and maternal health. *Fertil Steril* **103**,
668 1136-1143 (2015).
669 8. J. Balasch, E. Gratacos, Delayed childbearing: effects on fertility and the outcome of pregnancy.
670 *Curr Opin Obstet Gynecol* **24**, 187-193 (2012).
671 9. F. E. Duncan *et al.*, Age-associated dysregulation of protein metabolism in the mammalian oocyte.
672 *Aging Cell* **16**, 1381-1393 (2017).
673 10. N. Basisty, J. G. Meyer, B. Schilling, Protein Turnover in Aging and Longevity. *Proteomics* **18**,
674 e1700108 (2018).
675 11. E. F. Fornasiero *et al.*, Precisely measured protein lifetimes in the mouse brain reveal differences
676 across tissues and subcellular fractions. *Nat Commun* **9**, 4230 (2018).
677 12. E. F. Fornasiero, J. N. Savas, Determining and interpreting protein lifetimes in mammalian tissues.
678 *Trends Biochem Sci* **48**, 106-118 (2023).
679 13. E. Bomba-Warczak, S. L. Edassery, T. J. Hark, J. N. Savas, Long-lived mitochondrial cristae
680 proteins in mouse heart and brain. *J Cell Biol* **220**, (2021).
681 14. J. N. Savas, B. H. Toyama, T. Xu, J. R. Yates, 3rd, M. W. Hetzer, Extremely long-lived nuclear
682 pore proteins in the rat brain. *Science* **335**, 942 (2012).
683 15. B. H. Toyama *et al.*, Identification of long-lived proteins reveals exceptional stability of essential
684 cellular structures. *Cell* **154**, 971-982 (2013).
685 16. E. Bomba-Warczak, J. N. Savas, Long-lived mitochondrial proteins and why they exist. *Trends*
686 *Cell Biol* **32**, 646-654 (2022).
687 17. P. A. Hunt, T. J. Hassold, Human female meiosis: what makes a good egg go bad? *Trends Genet*
688 **24**, 86-93 (2008).
689 18. S. I. Nagaoka, T. J. Hassold, P. A. Hunt, Human aneuploidy: mechanisms and new insights into
690 an age-old problem. *Nat Rev Genet* **13**, 493-504 (2012).
691 19. F. Amargant *et al.*, Ovarian stiffness increases with age in the mammalian ovary and depends on
692 collagen and hyaluronan matrices. *Aging Cell* **19**, e13259 (2020).
693 20. S. M. Briley *et al.*, Reproductive age-associated fibrosis in the stroma of the mammalian ovary.
694 *Reproduction* **152**, 245-260 (2016).
695 21. J. H. Machlin *et al.*, Fibroinflammatory Signatures Increase with Age in the Human Ovary and
696 Follicular Fluid. *Int J Mol Sci* **22**, (2021).
697 22. H. M. Kinnear *et al.*, The ovarian stroma as a new frontier. *Reproduction* **160**, R25-R39 (2020).
698 23. B. F. Kimler *et al.*, Radiation-induced ovarian follicle loss occurs without overt stromal changes.
699 *Reproduction* **155**, 553-562 (2018).

24. R. Perrone *et al.*, CD38 regulates ovarian function and fecundity via NAD(+) metabolism. *iScience* **26**, 107949 (2023).
25. N. Quan *et al.*, Differential sensitivity of inbred mouse strains to ovarian damage in response to low-dose total body irradiationdagger. *Biol Reprod* **102**, 133-144 (2020).
26. M. L. Steinhauser, C. P. Lechene, Quantitative imaging of subcellular metabolism with stable isotopes and multi-isotope imaging mass spectrometry. *Semin Cell Dev Biol* **24**, 661-667 (2013).
27. C. Guillermier, M. L. Steinhauser, C. P. Lechene, Quasi-simultaneous acquisition of nine secondary ions with seven detectors on NanoSIMS50L: application to biological samples. *Surf Interface Anal* **46**, 150-153 (2014).
28. J. Nunez, R. Renslow, J. B. Cliff, 3rd, C. R. Anderton, NanoSIMS for biological applications: Current practices and analyses. *Biointerphases* **13**, 03B301 (2017).
29. C. Guillermier *et al.*, Imaging mass spectrometry demonstrates age-related decline in human adipose plasticity. *JCI Insight* **2**, e90349 (2017).
30. S. K. Park, J. D. Venable, T. Xu, J. R. Yates, 3rd, A quantitative analysis software tool for mass spectrometry-based proteomics. *Nat Methods* **5**, 319-322 (2008).
31. A. Rodriguez-Nuevo *et al.*, Oocytes maintain ROS-free mitochondrial metabolism by suppressing complex I. *Nature* **607**, 756-761 (2022).
32. K. Oktay, D. Briggs, R. G. Gosden, Ontogeny of follicle-stimulating hormone receptor gene expression in isolated human ovarian follicles. *J Clin Endocrinol Metab* **82**, 3748-3751 (1997).
33. P. P. Szotek *et al.*, Normal ovarian surface epithelial label-retaining cells exhibit stem/progenitor cell characteristics. *Proc Natl Acad Sci U S A* **105**, 12469-12473 (2008).
34. N. H. Thayer *et al.*, Identification of long-lived proteins retained in cells undergoing repeated asymmetric divisions. *Proc Natl Acad Sci U S A* **111**, 14019-14026 (2014).
35. J. N. Mara *et al.*, Ovulation and ovarian wound healing are impaired with advanced reproductive age. *Aging (Albany NY)* **12**, 9686-9713 (2020).
36. F. Paulini, R. C. Silva, J. L. Rolo, C. M. Lucci, Ultrastructural changes in oocytes during folliculogenesis in domestic mammals. *J Ovarian Res* **7**, 102 (2014).
37. J. J. Eppig, K. Wigglesworth, F. L. Pendola, The mammalian oocyte orchestrates the rate of ovarian follicular development. *Proc Natl Acad Sci U S A* **99**, 2890-2894 (2002).
38. A. J. Grootenhuis, H. L. Philipsen, J. T. de Breet-Grijsbach, M. van Duin, Immunocytochemical localization of ZP3 in primordial follicles of rabbit, marmoset, rhesus monkey and human ovaries using antibodies against human ZP3. *J Reprod Fertil Suppl* **50**, 43-54 (1996).
39. D. A. Gook, D. H. Edgar, J. Borg, M. Martic, Detection of zona pellucida proteins during human folliculogenesis. *Hum Reprod* **23**, 394-402 (2008).
40. N. F. Henning, R. D. LeDuc, K. A. Even, M. M. Laronda, Proteomic analyses of decellularized porcine ovaries identified new matrisome proteins and spatial differences across and within ovarian compartments. *Sci Rep* **9**, 20001 (2019).
41. T. Chiang, F. E. Duncan, K. Schindler, R. M. Schultz, M. A. Lampson, Evidence that Weakened Centromere Cohesion Is a Leading Cause of Age-Related Aneuploidy in Oocytes. *Curr Biol* **20**, 1522-1528 (2010).
42. J. Dong *et al.*, Ectopic expression of human TUBB8 leads to increased aneuploidy in mouse oocytes. *Cell Discov* **9**, 105 (2023).
43. R. Feng *et al.*, Mutations in TUBB8 and Human Oocyte Meiotic Arrest. *N Engl J Med* **374**, 223-232 (2016).
44. B. Nashun *et al.*, Continuous Histone Replacement by Hira Is Essential for Normal Transcriptional Regulation and De Novo DNA Methylation during Mouse Oogenesis. *Mol Cell* **60**, 611-625 (2015).
45. J. Uraji, K. Scheffler, M. Schuh, Functions of actin in mouse oocytes at a glance. *J Cell Sci* **131**, (2018).

749 46. X. Duan, S. C. Sun, Actin cytoskeleton dynamics in mammalian oocyte meiosis. *Biol Reprod* **100**,
750 15-24 (2019).
751 47. J. Roeles, G. Tsiavaliaris, Actin-microtubule interplay coordinates spindle assembly in human
752 oocytes. *Nat Commun* **10**, 4651 (2019).
753 48. A. Ajduk *et al.*, Rhythmic actomyosin-driven contractions induced by sperm entry predict
754 mammalian embryo viability. *Nat Commun* **2**, 417 (2011).
755 49. S. Dunkley, K. Scheffler, B. Mogessie, Cytoskeletal form and function in mammalian oocytes and
756 zygotes. *Curr Opin Cell Biol* **75**, 102073 (2022).
757 50. H. Diaz, P. Esponda, Ageing-induced changes in the cortical granules of mouse eggs. *Zygote* **12**,
758 95-103 (2004).
759 51. J. van der Reest, G. N. Cecchino, M. C. Haigis, P. Kordowitzki, Mitochondria: Their relevance
760 during oocyte ageing. *Ageing Res Rev* **70**, (2021).
761 52. G. C. Kujoth *et al.*, Mitochondrial DNA mutations, oxidative stress, and apoptosis in mammalian
762 aging. *Science* **309**, 481-484 (2005).
763 53. T. Wai *et al.*, The role of mitochondrial DNA copy number in mammalian fertility. *Biol Reprod*
764 **83**, 52-62 (2010).
765 54. E. Babayev, E. Seli, Oocyte mitochondrial function and reproduction. *Curr Opin Obstet Gynecol*
766 **27**, 175-181 (2015).
767 55. M. R. Chiaratti *et al.*, The role of mitochondria in the female germline: Implications to fertility
768 and inheritance of mitochondrial diseases. *Cell Biol Int* **42**, 711-724 (2018).
769 56. M. L. Steinhauser *et al.*, Multi-isotope imaging mass spectrometry quantifies stem cell division
770 and metabolism. *Nature* **481**, 516-519 (2012).
771 57. C. Guillermier, J. C. Poczatek, W. R. Taylor, M. L. Steinhauser, Quantitative imaging of
772 deuterated metabolic tracers in biological tissues with nanoscale secondary ion mass spectrometry.
773 *Int J Mass Spectrom* **422**, 42-50 (2017).
774 58. J. K. Eng, A. L. McCormack, J. R. Yates, An approach to correlate tandem mass spectral data of
775 peptides with amino acid sequences in a protein database. *J Am Soc Mass Spectrom* **5**, 976-989
776 (1994).
777 59. T. Xu *et al.*, ProLuCID: An improved SEQUEST-like algorithm with enhanced sensitivity and
778 specificity. *J Proteomics* **129**, 16-24 (2015).
779 60. D. Cociorva, L. T. D, J. R. Yates, Validation of tandem mass spectrometry database search results
780 using DTASelect. *Curr Protoc Bioinformatics* **Chapter 13**, Unit 13 14 (2007).
781 61. D. L. Tabb, W. H. McDonald, J. R. Yates, 3rd, DTASelect and Contrast: tools for assembling and
782 comparing protein identifications from shotgun proteomics. *J Proteome Res* **1**, 21-26 (2002).
783 62. J. Peng, J. E. Elias, C. C. Thoreen, L. J. Licklider, S. P. Gygi, Evaluation of multidimensional
784 chromatography coupled with tandem mass spectrometry (LC/LC-MS/MS) for large-scale protein
785 analysis: the yeast proteome. *J Proteome Res* **2**, 43-50 (2003).
786 63. M. J. MacCoss, C. C. Wu, H. Liu, R. Sadygov, J. R. Yates, 3rd, A correlation algorithm for the
787 automated quantitative analysis of shotgun proteomics data. *Anal Chem* **75**, 6912-6921 (2003).
788 64. H. Mi, A. Muruganujan, D. Ebert, X. Huang, P. D. Thomas, PANTHER version 14: more
789 genomes, a new PANTHER GO-slim and improvements in enrichment analysis tools. *Nucleic*
790 *Acids Res* **47**, D419-D426 (2019).
791